applied sciences

MDPI

Article

Synthesis and Printing Features of a Hierarchical Nanocomposite Based on Nickel–Cobalt LDH and Carbonate Hydroxide Hydrate as a Supercapacitor Electrode

Tatiana L. Simonenko [1], Nikolay P. Simonenko [1,*], Philipp Yu. Gorobtsov [1], Andrey S. Nikitin [2], Aytan G. Muradova [3], Yuri M. Tokunov [4], Stanislav G. Kalinin [5], Elizaveta P. Simonenko [1] and Nikolay T. Kuznetsov [1]

[1] Kurnakov Institute of General and Inorganic Chemistry, Russian Academy of Sciences, 31 Leninsky pr., Moscow 119991, Russia
[2] Department of Crystals Chemistry and Technology, Mendeleev University of Chemical Technology of Russia, 9 Miusskaya sq., Moscow 125047, Russia
[3] Department of Nanomaterials and Nanotechnology, Mendeleev University of Chemical Technology of Russia, 9 Miusskaya sq., Moscow 125047, Russia
[4] Moscow Institute of Physics and Technology, National Research University, 9 Institutskiy per., Dolgoprudny 141701, Russia
[5] Federal Research Center "Fundamentals of Biotechnology", Russian Academy of Sciences, Leninsky Prosp. 33-2, Moscow 119071, Russia
* Correspondence: n_simonenko@mail.ru

Abstract: The hydrothermal synthesis of a hierarchically organized nanocomposite based on nickel–cobalt carbonate hydroxide hydrate of composition $M(CO_3)_{0.5}(OH)\cdot 0.11H_2O$ (where M is Ni^{2+} and Co^{2+}) and nickel–cobalt layered double hydroxides (NiCo-LDH) was studied. Using synchronous thermal analysis (TGA/DSC), it was determined that the material retained thermal stability up to 200 °C. The crystal structure of the powder and the set of functional groups in its composition were determined by X-ray diffraction analysis (XRD) and Fourier transform infrared spectroscopy (FTIR). The resulting hierarchically organized nanopowder was employed as a functional ink component for microplotter printing of an electrode film, which is an array of miniature planar structures with a diameter of about 140 μm, on the surface of a nickel-plated steel substrate. Using scanning electron microscopy (SEM), it was established that the main area of the electrode "pixels" represents a thin film of individual nanorods with periodic inclusions of larger hierarchically organized spherical formations. According to atomic force microscopy (AFM) data, the mean square roughness of the material surface was 28 nm. The electrochemical properties of the printed composite film were examined; in particular, the areal specific capacitance at different current densities was calculated, and the electrochemical kinetics of the material was studied by impedance spectroscopy. It was found that the electrode material under study exhibited relatively low R_s and R_{ct} resistance, which indicates active ion transfer at the electrode/electrolyte interface.

Keywords: carbonate hydroxide hydrate; layered double hydroxides; NiCo-LDH; nanocomposite; hydrothermal synthesis; hierarchical structure; film; microplotter printing; supercapacitor

Citation: Simonenko, T.L.; Simonenko, N.P.; Gorobtsov, P.Y.; Nikitin, A.S.; Muradova, A.G.; Tokunov, Y.M.; Kalinin, S.G.; Simonenko, E.P.; Kuznetsov, N.T. Synthesis and Printing Features of a Hierarchical Nanocomposite Based on Nickel–Cobalt LDH and Carbonate Hydroxide Hydrate as a Supercapacitor Electrode. *Appl. Sci.* **2023**, *13*, 5844. https://doi.org/10.3390/app13105844

Academic Editors: Elena Korznikova and Andrey Kistanov

Received: 5 April 2023
Revised: 1 May 2023
Accepted: 5 May 2023
Published: 9 May 2023

1. Introduction

The steadily growing global demand for electricity, as well as the annually aggravating climatic problems, require the creation of alternative devices not only for generating "green" electricity but also for its distribution and storage. A promising technology for solving the challenges of energy storage and accumulation is the creation of commercially available supercapacitors with high capacity, high speed, and long service life [1–4]. However, despite the significant amount of research devoted to this topic, to date, there are very few papers reporting on the development of such devices that have all of the above advantages simultaneously [5,6]. The fulfillment of such an ambitious task requires the creation of

new electrode materials with high electrocatalytic activity and conductivity, as well as a developed specific surface area, in addition to improving the engineering and technological approaches to design and assembly. In addition, it is noted that the electrode materials should have a medium degree of crystallinity because well-crystallized structures have no ability to expand or contract during supercapacitor operation, which prevents the penetration of protons deep into the material and leads to diffusion difficulties, while amorphous materials demonstrate low values of electrical conductivity [7,8].

In recent years, various classes of transition metal compounds (Ni, Co, Mn, Fe, Mo, and V), in particular, oxides [9,10], hydroxides [11,12], hydroxocarbonates [7,13], sulfides [14–16], phosphates [17,18], and composites based on them [19–21], have been considered as candidates for the role of supercapacitor electrodes with a pseudocapacitative effect. According to literature data [22–24], the layered hydroxides and carbonate hydroxide hydrates of nickel and cobalt are of particular interest from this point of view, since wide interplanar distance in their crystal structure can greatly facilitate the access of electrolyte ions into the inner structure of the material, increasing the number of active centers involved in the electrode. Furthermore, it is reported that $Co(CO_3)_{0.5}(OH)$ contains additional internal metallic bonds in its structure that promote electron transport and improve the conductivity of the final electrode [24]. Moreover, the presence of CO_3^{2-} groups in the composition of layered carbonate hydroxide hydrates increases the hydrophilicity of the material, which also has a positive effect on the rate of electron diffusion in its structure [25]. Thus, the formation of nanocomposites based on layered hydroxides and carbonate hydroxide hydrates of nickel and cobalt can contribute to combining their useful characteristics and obtaining new electrode materials with improved operating parameters. The most convenient method for obtaining such compounds is hydrothermal synthesis [26–28], which allows, depending on the process conditions (concentration and type of reagents, temperature and pressure in the reactor, and the duration of thermal treatment), one to obtain a wide range of microstructure variants with varying degrees of dispersity and crystallinity. Additionally, this method allows hierarchically organized materials and films to be formed with increased roughness, which ensures better wettability of the material surface and increases its specific surface area and the number of active centers, contributing to fast ion diffusion at higher applied current and therefore ensuring a high-rate performance [29–31].

In most works concerning the development of supercapacitor electrodes, the application of the active material is most often carried out by impregnating the carrier, by screen printing with pastes based on the target material and organic binder [7,24,32], or in the process of hydrothermal growth of films, directly on the surface of substrates of varying nature [33–35]. These approaches are not always convenient from the point of view of targeted material deposition or creation of electrode structures of complex geometry; in addition, removal of the organic binder after coating deposition requires additional heat treatment of the obtained samples, which may negatively affect their morphology, chemical composition, or crystal structure. Previous research by various authors has shown the high efficiency of using printing technology to create miniaturized components and devices for alternative energy, electronics, and gas sensing. In particular, it has been demonstrated that approaches such as ink-jet printing [36–39], aerosol printing microplotter [40–43] and microextrusion [44–49] printing, and pen plottier printing [50–52] allow the use of inks of varied viscosity, forming coatings of different thickness and geometry with high accuracy and ensuring high reproducibility of microstructures and functional characteristics of the resulting planar structures.

The purpose of this work was to study the synthesis of a nanocomposite based on layered double nickel and cobalt hydroxides and carbonate hydroxide hydrates by using a hydrothermal process to develop a technique for the microplotter printing of an electrode film as an array of miniature planar nanostructures on a nickel-plated steel surface using functional inks based on the obtained hierarchically organized powder and

to study the electrochemical properties of the resulting material as a promising component of supercapacitors.

2. Materials and Methods

2.1. Materials

$NiCl_2 \cdot 6H_2O$ (>98%, Lenreactiv, St. Petersburg, Russia), $Co(NO_3)_2 \cdot 6H_2O$ (>98%, Lenreactiv, St. Petersburg, Russia), $(NH_2)_2CO$ (99%, RUSHIM, Moscow, Russia), and ethylene glycol (Chimmed, Moscow, Russia) were used in this work without further purification.

2.2. Nanopowder Preparation

Powder preparation was carried out using a hydrothermal process. Firstly, an aqueous solution of nickel chloride and cobalt nitrate (volume of 60 mL and a total metal concentration of 0.05 mol/L, n(Co)/n(Ni) = 2) was prepared. Then, 0.63 g of urea was added to this solution, and the resulting reaction system was placed in a 100 mL stainless-steel autoclave with a Teflon insert followed by controlled heat treatment in a muffle furnace (temperature—140 °C, duration of heat treatment—1 h, and heating rate—1.5 °C/min). After natural cooling, the formed solid phase particles were separated and washed with distilled water by cyclic centrifugation. Finally, the obtained powder was dried at 100 °C for 5 h and further characterized using a set of methods of physico-chemical analysis.

2.3. Microplotter Printing of Electrode Film

The resulting hierarchically organized nanopowder was used to prepare a stable disperse system (solid phase particle content of 10 mg) in ethylene glycol (1 mL volume), with rheological properties suitable for serving as a functional ink for microplotter printing an array of miniature planar nanostructures on the surface of a nickel-plated steel substrate (substrate dimensions 25 × 8 × 0.15 mm). A capillary with a channel diameter of 120 μm was used as a dispenser. Automatic application of an array of miniature planar nanostructures (lateral dimensions of the modified substrate surface were 10 × 8 mm, and the distance between individual pixels was 300 μm) to both sides of the substrate was performed using a 3-axis positioning system after a meniscus of functional ink touched the substrate surface according to a digital trajectory. The formed ink film was further subjected to step drying in the temperature range of 25–100 °C (2 h) to evaporate the solvent. Thus, arrays of 858 pixels (a total of 1716 pixels) of electrode material were formed on both substrate surfaces. Considering that the volume of one drop of ink during printing was about 1.4 nL, the total mass of the active material deposited on the surface of the substrate was 2.5–10^{-5} g.

2.4. Instrumentation

The thermal behavior of the obtained semiproduct was studied using synchronous (TGA/DSC) thermal analysis (SDT Q-600 thermal analyzer, TA Instruments, New Castle, DE, USA) in an air flow in the temperature range of 25–1000 °C (controlled heating was performed in Al_2O_3 microcrucibles at the rate of 10 °/min in air flow, the gas flow rate was 250 mL/min, and the sample mass was 8.911 mg).

To record the Fourier transform infrared (FTIR) spectra of the powder, a suspension was prepared in nujol mull, which was then placed as a film between KBr glasses. Spectra were recorded in the wave number range of 350–4000 cm^{-1} (signal accumulation time—15 s and resolution—1 cm^{-1}) using an FTIR spectrometer InfraLUM FT-08 (Lumex, St. Petersburg, Russia).

XRD analysis of the obtained powder was carried out using a D8 Advance diffractometer (Bruker, Bremen, Germany; CuKα = 1.5418 Å, Ni filter, E = 40 keV, I = 40 mA, 2θ range—5°–80° and 30°–41°, resolution—0.02°, signal accumulation time at one point was 0.3 s and

2.0 s (in the case of powder analysis at 2θ range—30°–41°)). The average size of the coherent scattering region (CSR) was calculated using the Debye–Scherrer formula [53]:

$$D = \frac{k\lambda}{\beta cos\theta}, \quad (1)$$

with D being crystallite size, λ being X-ray wavelength, k being Scherrer's constant, β being the full width at half maximum, and θ being the diffraction angle.

The microstructures of the obtained nanopowder and the formed array of miniature planar nanostructures were studied using scanning electron microscopy (SEM; NVision-40, Carl Zeiss, Inc., Oberkochen, Germany). Elemental analysis and mapping of element distributions over the film surface were performed as part of SEM by using an EDX spectrometer INCA X-MAX 80 (Oxford Instruments, Abingdon, UK).

The film applied to the surface of the nickel-plated steel substrate was also examined by atomic force microscopy (AFM). As a result of the performed measurements, the data on the film microstructure and its local electrophysical properties were obtained. For this purpose, a Solver Pro-M scanning probe microscope (NT-MDT, Zelenograd, Russia) and ETALON HA-HR probes (ScanSens, Bremen, Germany) with W_2C+ conductive coating (tip curvature radius < 35 nm) in modes of semicontact AFM, Kelvin probe force microscopy (KPFM), and scanning capacitive microscopy (SCM) were used. The measurements were performed at ambient conditions.

The electrochemical characteristics of the sample were investigated using a potentiostat-galvanostat P-40X equipped with an electrochemical impedance measurement module FRA-24M (Electrochemical Instruments, Chernogolovka, Russia) at room temperature (25 °C). The material printed on the surface of a nickel-plated steel substrate served as the working electrode, and Ag/AgCl and a graphite rod were used as the reference and counter electrodes, respectively. The mass of the active material was 2.5×10^{-5} g. The measurements were carried out by cyclic voltammetry (CVA), galvanostatic charge–discharge (GCD), and electrochemical impedance spectroscopy (EIS) in the electrolyte, which was an aqueous solution of KOH (c = 3 mol/L). The value of the areal specific capacitance (C_s, F/cm^2) of the electrode material under study was calculated using the discharge curves measured using the three-electrode scheme according to the following formula [54]:

$$C_s = (I \times \Delta t)/(S \times \Delta V) \quad (2)$$

where I is the discharge current (A), Δt is the discharge time (s), ΔV is the discharge potential window, and S is the geometric area of the electrode (cm^2).

3. Results and Discussion

3.1. Characterization of the Prepared Nanopowder

The thermal stability of the obtained powder was studied by means of a synchronous thermal analysis (Figure 1). As can be seen from the corresponding thermograms, the material undergoes 3 stages of mass loss in the investigated temperature range in the intervals 25–220, 220–410, and 410–860 °C. In the 1st stage, the value of mass loss is about 6%, which is associated with the removal of residual solvent and sorbed atmospheric gases. The 2nd stage shows a more intense mass reduction (Δm = 20.5%), accompanied by a more complex set of thermal effects. As can be seen from the DSC curve, in this case, there is a combination of endothermic effects in the region of 225–370 °C with a narrower exo-effect and a maximum at 265 °C. This behavior is characteristic of the carbonate hydroxide hydrate of cobalt of the composition $Co(CO_3)_{0.5}(OH)\cdot 0.11H_2O$ [55] and may be associated with the oxidation process $Co^{2+} \rightarrow Co^{3+}$ as well as with crystallization of the corresponding oxide. The simultaneous presence of intense mass loss and thermal effects with energy absorption indicates active decomposition of the substance in a given temperature interval. This process continues even at further temperature increases, but its rate decreases significantly. The value of Δm at the third stage is about 5.5%, and at its final stage, an acceleration

of the mass reduction process is observed, accompanied by an endothermic effect with a minimum around 838 °C associated with the decomposition of $NiCo_2O_4$ oxide formed in the temperature range of 400–500 °C. The powder mass stabilizes with a further increase in temperature. Thus, the total mass loss in the investigated temperature range was about 32%. Taking into account the results of the analysis, the thermal stability of the powder under study is limited to a temperature of about 200 °C.

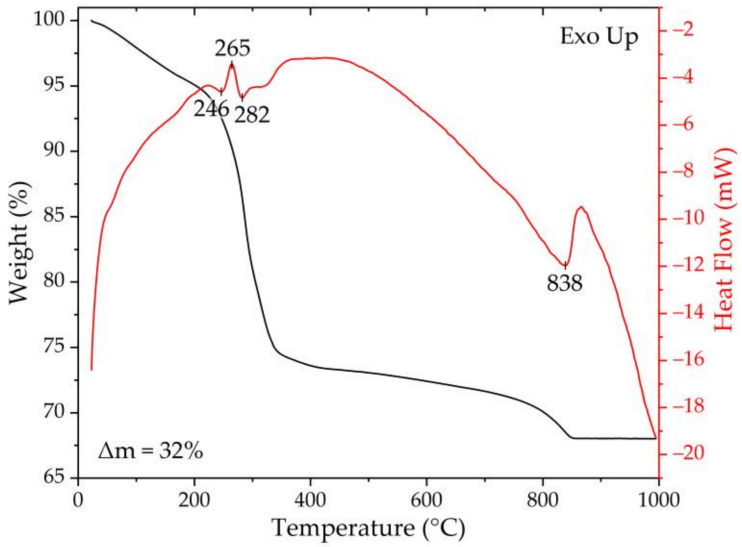

Figure 1. Results of synchronous (TGA/DSC) thermal analysis of the obtained powder.

The crystalline structure of the obtained powder was studied using X-ray powder diffraction analysis (XRD) (Figure 2). As can be seen from the overview diffractogram, the powder is characterized by a fairly low degree of crystallinity, which, as we noted earlier, is preferable for supercapacitor electrodes, contributing to a more effective penetration of charged particles deep into the material and interaction with a greater number of active centers on its surface. Nevertheless, the analysis results allow us to observe the simultaneous presence of a set of reflexes characteristic of nickel–cobalt carbonate hydroxide hydrate of composition $M(CO_3)_{0.5}(OH)\cdot 0.11H_2O$ (where M is Ni^{2+} and Co^{2+}) (JCPDS card no. 48-0083) [56,57] and a signal at 2θ = 12.2°, probably related to (003) planes of the hydrotalcite-like nickel–cobalt layered double hydroxides phase (JCPDS card no. 33-0429) [53,58] on the XRD pattern. The main component in the composite thus formed is nickel–cobalt carbonate hydroxide hydrate, so in the first place, the following chemical interactions took place in the hydrothermal synthesis stage [56]:

$$H_2O + CO(NH_2)_2 \rightarrow CO_2 + 2NH_3 \quad (3)$$

$$H_2O + CO_2 \rightarrow 2H^+ + {CO_3}^{2-} \quad (4)$$

$$0.11H_2O + M^{2+} + OH^- + 0.5{CO_3}^{2-} \rightarrow M(CO_3)_{0.5}(OH)\cdot 0.11H_2O \quad (5)$$

The average crystallite size for the obtained $M(CO_3)_{0.5}(OH)\cdot 0.11H_2O$, according to the analysis of XRD data, was 26 ± 3 nm.

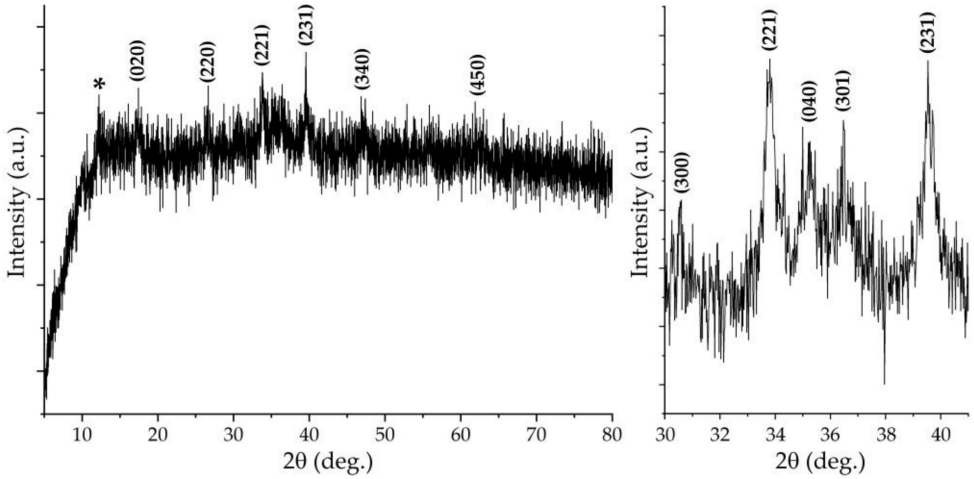

Figure 2. XRD patterns of the obtained powder (left—overview and right—for 2θ range 30°–41° with longer signal accumulation; reflex from the nickel–cobalt layered double hydroxides phase is marked by the "*" marker).

FTIR spectroscopy was employed to study the set of functional groups in the synthesized sample composition (Figure 3). The spectral analysis findings agree well with the XRD data, which is confirmed by the presence of absorption bands associated with the above-mentioned components. Thus, the absorption band around 1530 cm^{-1} partially overlapping with the signal from the Vaseline oil belongs to the $\nu(OCO_2)$ stretching vibration. The low-intensity bands at 1070 and 829 cm^{-1} are related to ν(C=O) and $\delta(CO_3)$, respectively, and the bands with maxima at 968 and 528 cm^{-1} are attributed to δ(M–OH) and ρ_w(Co–OH), respectively. The indicated absorption band set is characteristic of carbonate hydroxide hydrate [56]. The broad absorption band in the 3100–3700 cm^{-1} region probably refers to the ν(O–H) stretching vibration of NiCo-LDH, and the weak signal around 1640 cm^{-1} refers to the bending vibration, which is typical for layered metal hydroxides [59,60]. The spectrum of the composite powder under study also exhibits an absorption band in the region of 2150–2260 cm^{-1}, probably related to ν(NCO) vibrations [61]. The presence of this functional group may be connected with the formation of isocyanic acid during urea decomposition during hydrothermal treatment of the reaction system [62] in accordance with the following reaction:

$$NH_2—CO—NH_2 \rightarrow NH_3 + HNCO \quad (6)$$

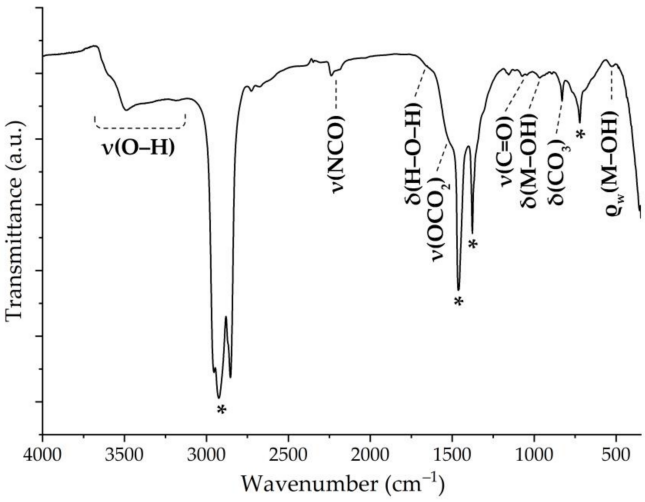

Figure 3. FTIR spectrum of the obtained powder (the "*" marker indicates Vaseline oil absorption bands).

Furthermore, the incorporation of the –NCO group into the material structure is common to layered hydroxides due to the peculiarities of their structure, as follows from the FTIR results of other authors [32] who used urea as a precipitant in the synthesis of NiCo-LDH. Thus, the presence of the corresponding absorption band in the spectrum of the powder we obtained provides additional evidence for the presence of nickel–cobalt layered double hydroxides as a material component.

The microstructure of the obtained powder was examined by SEM (Figure 4). The corresponding images demonstrate the presence of two structures in the material. The first is a spherical hierarchically organized structure with a diameter of 8–10 μm, whose surface consists of orthogonally arranged nanorods about 1 μm long and 10–50 nm thick, which agrees well with the results of the average CSR size estimation. Individual nanorods of similar size or agglomerates in the form of bundles consisting of several nanorods should be noted as the second component. The presence of two microstructural types agrees well with the XRD and FTIR powder results, which indicate the simultaneous presence of nickel–balt carbonate hydroxide hydrate $M(CO_3)_{0.5}(OH)\cdot 0.11H_2O$ (where M is Ni^{2+} and Co^{2+}) and nickel–cobalt layered double hydroxides in the material composition. Given the literature data, the hierarchically organized spherical formations probably belong to nickel–cobalt carbonate hydroxide hydrate [63], while individual nanofibers and their bundles can be attributed to NiCo-LDH. Thus, the results of scanning electron microscopy further confirm the composite nature of the obtained nanopowder.

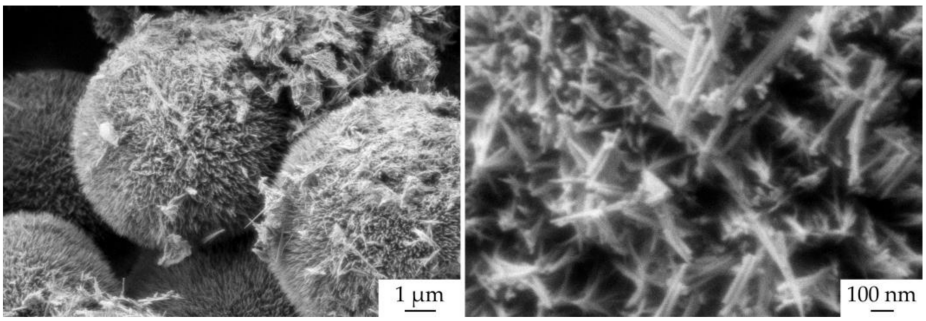

Figure 4. Microstructure of the obtained nanopowder (according to SEM data).

3.2. Characterization of the Printed ($M(CO_3)_{0.5}(OH)\cdot 0.11H_2O$)/(NiCo-LDH) Film

Functional inks obtained from the hierarchically organized ($M(CO_3)_{0.5}(OH)\cdot 0.11H_2O$)/(NiCo-LDH) (where M is Ni^{2+} and Co^{2+}) nanopowder were further used for the microplotter printing of an electrode film on the surface of a nickel-plated steel substrate on both sides (Figure 5a). The appearance of the resulting sample allows one to observe the formed ordered array of miniature planar nanostructures ("pixels") with a distance of 300 μm between their centers (Figure 5b,c), which additionally testifies to the high addressability of material deposition and reproducibility of the electrode structure formation process using printing technologies.

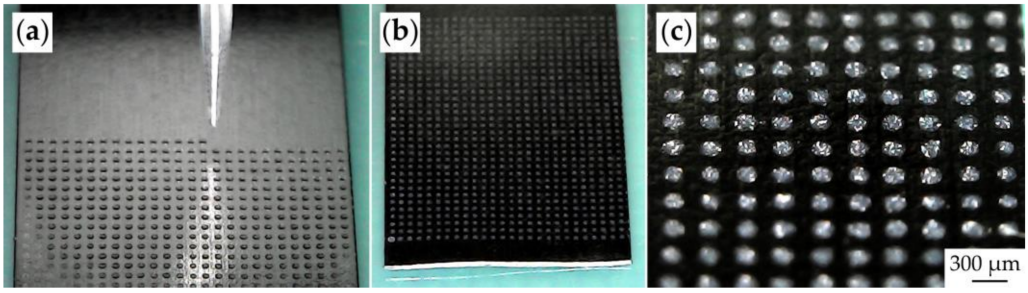

Figure 5. The microplotter printing of functional film (**a**) and the appearance of the resulting miniature planar nanostructure array on a Ni substrate (**b**,**c**).

When studying the microstructural features of the printed film by SEM, maps of element (Ni, Co, and O) distribution over the studied sample surface were built (Figure 6). The results clearly demonstrate the reduced content of nickel in the formed miniature planar nanostructures compared to the substrate surface. In the electrode "pixels" area, the presence of cobalt and increased oxygen concentration compared to the surface of the metal substrate are also observed.

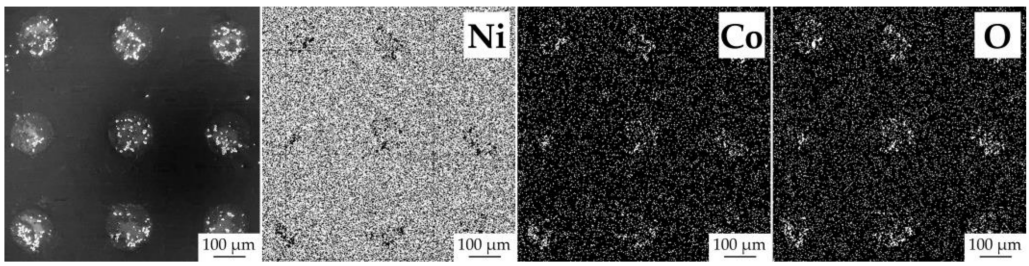

Figure 6. Printed film microstructure and element distribution maps (Ni, Co, and O) on its surface.

A more detailed analysis of the printed film microstructure showed that the diameter of individual miniature planar structures is about 140 µm (Figure 7a). As can be seen from the micrograph of an individual "pixel", the gradient of particle distribution over the surface (coffee stain effect) is almost absent (Figure 7b). The main area of printed planar structures is a thin film of individual nanorods with periodic inclusions of larger spherical hierarchically organized formations (Figure 7c). Therefore, the microstructural features of the $(M(CO_3)_{0.5}(OH)\cdot 0.11H_2O)/(NiCo\text{-}LDH)$ (where M is Ni^{2+} and Co^{2+}) composite powder are preserved during functional ink preparation and electrode film application. Thus, the spherical formations, as in the case of the powder, consist of nanorods orthogonally arranged to their outer surface (Figure 7d–f), and the individual nanorods covering the main surface of the electrode "pixels" are 10–50 nm thick (Figure 7g–i).

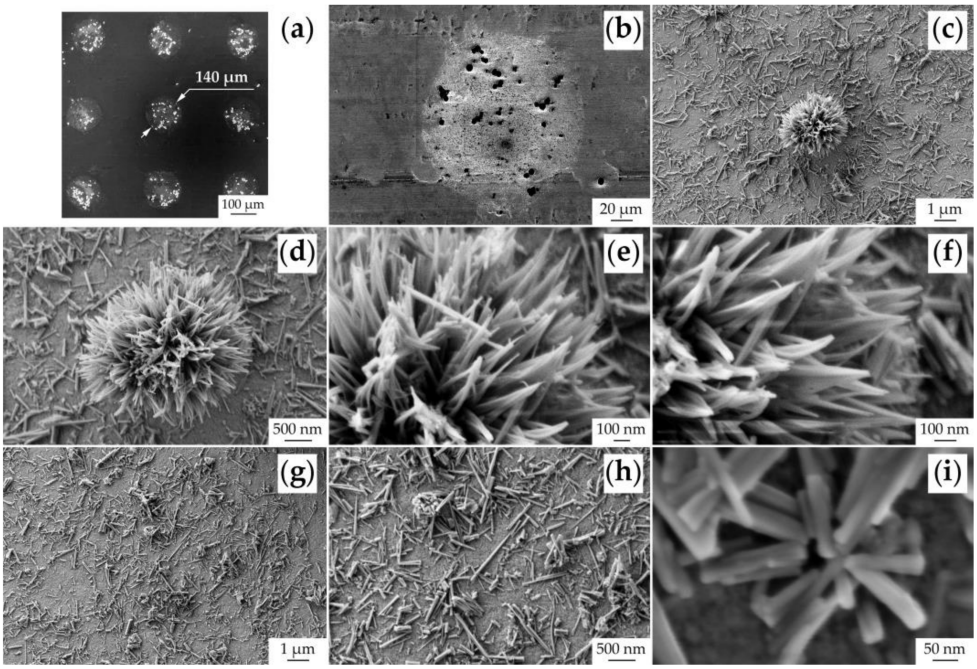

Figure 7. Microstructure of the printed film (according to SEM data).

The results of AFM analysis of the film surface (Figure 8a,b) show that the main surface of the formed miniature planar nanostructures consists of anisotropic one-dimensional particles with a thickness of about 35 nm and a submicron length (400–1200 nm). At the

same time, there is a tendency for the combination of the particles by side faces, forming agglomerates in the shape of "stacks". This film microstructure agrees well with the SEM results. In order to visualize the obtained film topography, the corresponding 3D images are given in Figure 8e,f. The mean square roughness of the material surface is 28 nm (for a pure substrate, this parameter is 8 nm). This value is close to the thickness of one-dimensional particles, which indicates the formation of an active electrode layer with a thickness comparable to that of a single particle.

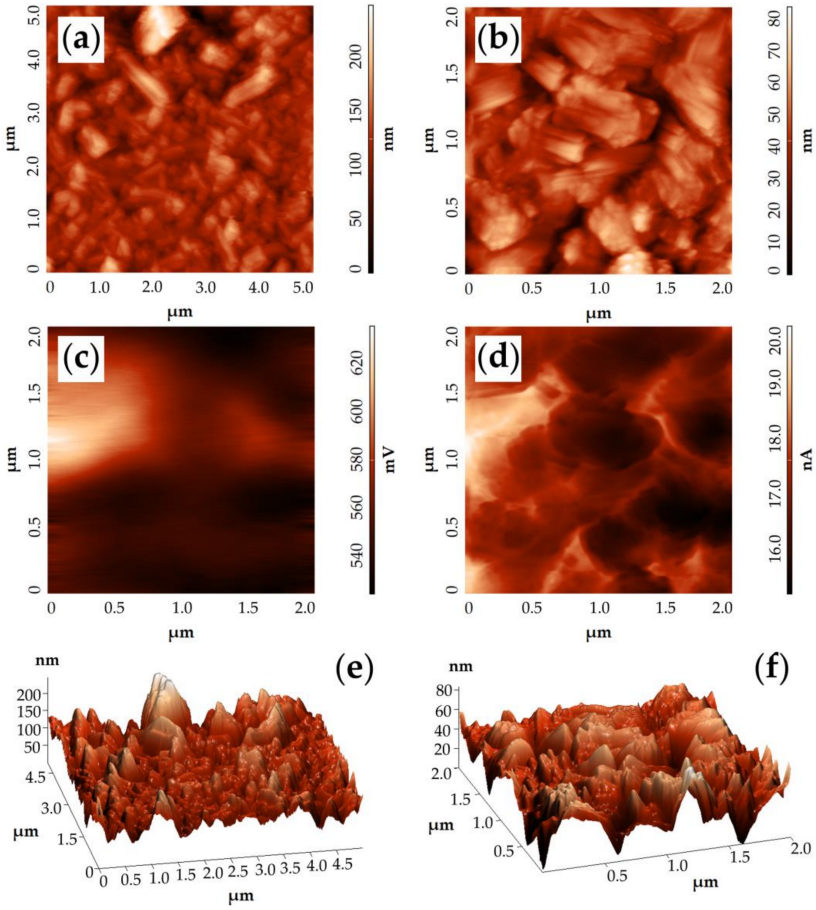

Figure 8. AFM results of the nickel–cobalt carbonate hydroxide hydrate film: topography (**a**,**b**), surface potential distribution map (**c**), capacity gradient distribution map for "probe tip—sample microregion" capacitor (**d**), and 3D images of the film at different magnifications (**e**,**f**).

During the study of the film surface, its local electrophysical properties were also studied (Figure 8c,d). Thus, the surface potential distribution map (Figure 8c) shows areas with markedly higher values of this parameter (~0.1 eV). This may indicate that the film has insufficient conductivity (probably related to the lack of dense contact between the particles) for a uniform distribution of charges over its surface, resulting in the formation of areas with strongly prominent surface charges. On the map of capacitance gradient distribution over the material surface of the "probe tip—sample microregion" capacitor (Figure 8d), the boundaries between particles are practically not distinguished, which can also indicate a slightly reduced electronic conductivity or that its intergrain character is not strongly pronounced.

Using a probe with a known electron work function (ϕ_{wt} = 4.683 eV) calibrated with highly oriented pyrolytic graphite, the value of the electron work function for the film surface was determined to be 4.13 eV from the KPFM results. For NiCo-LDH-based materials, this value in the literature ranges from 2.9–2.97 [64,65] to 4.2 [66] and 5.24 eV [67]. Such a wide range of values of the electron work function may indicate a significant

influence on this parameter of not only the chemical composition but also the synthesis conditions and microstructural features of the material, which confirms the need for additional systematic studies.

3.3. Electrochemical Properties

The CV curves presented in Figure 9a regardless of the scan rate exhibit two pronounced redox peaks in the 0–0.5 V (vs. Ag/AgCl) potential region. This form of the curve indicates that the electrochemical capacity of the studied sample is mostly determined by the faradaic processes' contribution. The reversible transformations of electrode material occurring during electrochemical testing proceed in two stages: at the first stage, carbonate hydroxide hydrates of nickel and cobalt are transformed into metahydroxides (reactions 7 and 8 [25,68]), followed by the appearance of reversible transitions $Ni^{2+} \leftrightarrow Ni^{3+}$ and $Co^{2+} \leftrightarrow Co^{3+} \leftrightarrow Co^{4+}$ (reactions 9–11 [69]):

$$Ni_2(CO_3)(OH)_2 + 4OH^- \leftrightarrow 2NiOOH + CO_3^{2-} + 2H_2O + 2e^- \quad (7)$$

$$Co_2(CO_3)(OH)_2 + 4\,OH^- \leftrightarrow 2CoOOH + CO_3^{2-} + 2H_2O + 2e^- \quad (8)$$

$$NiOOH + H_2O + e^- \leftrightarrow Ni(OH)_2 + OH^- \quad (9)$$

$$CoOOH + H_2O + e^- \leftrightarrow Co(OH)_2 + OH^- \quad (10)$$

$$CoOOH + OH^- \leftrightarrow CoO_2 + H_2O + e^- \quad (11)$$

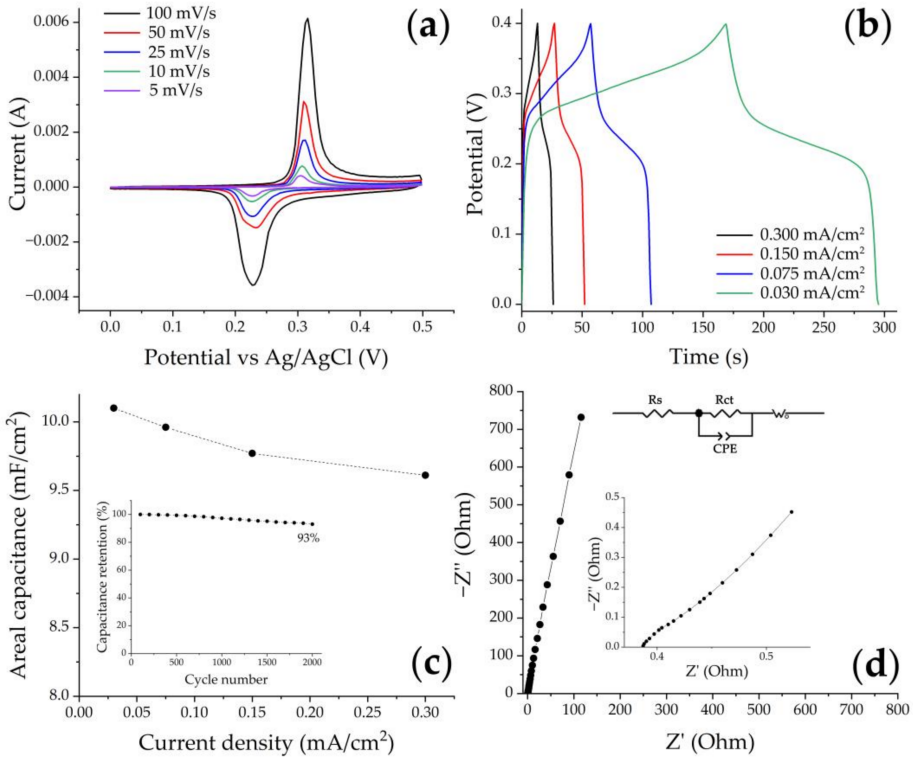

Figure 9. Electrochemical performance of materials in a three-electrode system with 3 M KOH electrolyte: CV curves at different scan rates (**a**), GCD curves at different current densities (**b**) and rate capabilities (inset: cycle performance of the film at 0.300 mA/cm^2 for 2000 cycles) (**c**), and the EIS spectrum for the material under study (inset: enlargement of high-frequency part and equivalent circuit model) (**d**).

Since the nickel and cobalt redox processes have sufficiently close potential ranges, in our case, they probably overlap, and only two distinct peaks are observed on the CV curves. It should be noted that the shape of the curves remained practically unchanged as the scanning speed increased; only a slight shift of the anodic peaks towards more positive potential and cathodic peaks towards more negative potential was observed, which was additionally accompanied by the increase in the current value. This trend indicates the energy storage possibility, as well as the reproducibility and reversibility of the processes that cause the occurrence of the material electrochemical capacitance [69].

According to the galvanostatic charge–discharge tests at different current densities, the discharge curves were plotted (Figure 9b), which have a non-linear range and a plateau, which agrees well with the CV curves and further confirms the faradaic mechanism of capacitance in the studied sample. Based on the GDC data, and using Equation (2), the areal specific capacitance (C_s) values were calculated, and it was found that increasing the current density from 0.030 mA/cm^2 to 0.300 mA/cm^2 leads to a 5% decrease in the C_s value from 10.1 to 9.6 mF/cm^2 (Figure 9c). Such a decrease in capacitance is typical for supercapacitor electrodes and related to the fact that at higher current densities, electrolyte ions involved in the charge transfer process do not have time to penetrate into the material pores and interact only with a limited number of the surface active centers, while at lower density, the charged particles reach a greater material depth, providing the most effective interaction of electrolyte with active centers of the surface. Cyclic stability tests of the investigated electrode material allowed us to determine that the capacitance value at 0.300 mA/cm^2 is retained by 93% after 2000 charge–discharge cycles (Figure 9c, inset). Such stability has been previously observed for similar materials and may be due to the presence of nanorod structures in their composition, which, as shown in [28], enable stabilization of the active material volume change in the process of hydroxide-ion incorporation/extraction according to reactions 9–11.

The electrochemical characteristics of the pristine substrate without active material were additionally studied (Figure S1a,b). The CV curves show that the current values as well as the CV-integrated area in the case of a pure substrate are several times smaller compared to the substrate with nanostructures printed on its surface. The capacitance value of the pure substrate calculated with the galvanostatic charge–discharge data was about 3.5 mA/cm^2 at 0.030 mA/cm^2, which is about 3 times lower than the capacitance value for the studied electrode.

Additionally, the electrochemical kinetics of the obtained electrode was studied by impedance spectroscopy. The corresponding Nyquist plot (Figure 9d) includes two components: a semicircle (in the high-frequency range) and a straight line (in the low-frequency range). The diameter of the semicircle represents the charge transfer resistance (R_{ct}), and the interval cut by the curve at high frequencies from the real axis indicates the diffusion or solution resistance (R_s) of the electrolyte [70]. The electrode material under study exhibits relatively low R_s (0.386 Ohm) and R_{ct} (1.6 Ohm) resistances, indicating active ion transport at the electrode/electrolyte interface. The Nyquist plot under consideration also contains a linear part described by the Warburg impedance (Figure 9d, inset), which determines the electrolyte ion penetration into the active material of the electrode [70].

Analyzing the obtained functional characteristics of the formed electrode material, one can judge that the demonstrated specific capacitance values are generally comparable with similar materials (Table S1) obtained earlier by other researchers when creating the miniature supercapacitor electrodes [31,71,72]. In addition, it is important to note the high cyclic stability of the electrode material obtained in our study, which is important in terms of the final device lifetime. Further increases in the specific capacitance value of the electrode material we proposed could be achieved by increasing the active material mass as well as the substrate surface area modified by it. Nevertheless, in the course of the study, it was shown that the proposed technology of synthesis and printing gives a fundamental possibility for the effective formation of the corresponding miniature electrode nanostructures as promising components of miniature supercapacitors. The results of the

electrochemical characteristics comparison of the materials obtained by us with similar ones obtained in other works are given in Table S1 in the Supplementary Materials.

4. Conclusions

The hydrothermal synthesis of a hierarchically organized nanocomposite based on nickel–cobalt carbonate hydroxide hydrate of composition $M(CO_3)_{0.5}(OH)\cdot 0.11H_2O$ (where M is Ni^{2+} and Co^{2+}) and nickel–cobalt layered double hydroxides was studied. TGA/DSC results indicated that the prepared material retained thermal stability up to 200 °C. The XRD and FTIR data revealed the main component of the material to be nickel–cobalt carbonate hydroxide hydrate, and the presence of NiCo-LDH was further confirmed by the presence of an –NCO group intercalated in its structure, formed by the urea decomposition under hydrothermal conditions. The resulting hierarchically organized nanopowder was utilized for functional ink fabrication and electrode film printing on the surface of a nickel-plated steel substrate. Analysis of its microstructure showed that the diameter of individual miniature planar structures is about 140 μm. Furthermore, it was demonstrated that the microstructural features of the nanocomposite after the functional film application are preserved—the main area of the printed miniature planar structures is a thin film of individual nanorods 10–50 nm thick (which agrees well with the calculated average CSR size: D = 26 ± 3 nm) with periodic inclusions of larger hierarchically organized spherical formations 8–10 μm in diameter calculated from XRD data. The AFM data indicated that the mean square roughness of the material surface was 28 nm, and the work function value of the surface of the miniature electrode structure (4.13 eV) was estimated according to the KPFM results. The electrochemical properties were studied for the formed composite film; in particular, the specific capacitance was determined, and it was found that a decrease in current density from 0.300 mA/cm^2 to 0.030 mA/cm^2 leads to an increase in this parameter from 9.6 to 10.1 mF/cm^2. The electrochemical kinetics of the obtained electrode was investigated by impedance spectroscopy. As a result, it was found that the examined electrode material exhibited relatively low R_s and R_{ct} resistance, which indicates active ion transfer at the electrode/electrolyte interfaces. Thus, the study showed that the hydrothermal method allowed us to prepare a hierarchically organized nanocomposite based on nickel–cobalt carbonate hydroxide hydrate of composition $M(CO_3)_{0.5}(OH)\cdot 0.11H_2O$ (where M is Ni^{2+} and Co^{2+}) and NiCo-LDH, and through microplotter printing, the targeted and reproducible formation of corresponding miniature electrode nanostructures as promising components of compact supercapacitors can be realized.

Supplementary Materials: The following supporting information can be downloaded at: https://www.mdpi.com/article/10.3390/app13105844/s1, Figure S1: Electrochemical characterization of initial nickel-plated steel substrate: CV curves at various scan rates (a) and GCD curves at various current densities (b); Table S1: Comparison of areal capacitance and cycle stability of different Ni-based electrode materials for micro-supercapacitors.

Author Contributions: Conceptualization, N.P.S. and T.L.S.; validation, N.P.S., E.P.S. and N.T.K.; investigation, T.L.S., A.G.M., N.P.S., P.Y.G., Y.M.T. and S.G.K.; writing—original draft preparation, T.L.S., P.Y.G., A.S.N., A.G.M., E.P.S., N.P.S. and N.T.K.; writing—review and editing, T.L.S., N.P.S., Y.M.T. and S.G.K.; visualization, T.L.S., A.S.N., N.P.S. and P.Y.G.; supervision, N.P.S., E.P.S. and N.T.K.; funding acquisition, Y.M.T. All authors have read and agreed to the published version of the manuscript.

Funding: This work was supported by the Ministry of Science and Higher Education of the Russian Federation (state contract no. 075-03-2023-106, project identifier 0714-2020-0007).

Institutional Review Board Statement: Not applicable.

Informed Consent Statement: Not applicable.

Data Availability Statement: Not applicable.

Conflicts of Interest: The authors declare no conflict of interest.

References

1. Xiong, C.; Wang, T.; Zhao, Z.; Ni, Y. Recent progress in the development of smart supercapacitors. *SmartMat* **2023**, *4*, e1158. [CrossRef]
2. Oyedotun, K.O.; Ighalo, J.O.; Amaku, J.F.; Olisah, C.; Adeola, A.O.; Iwuozor, K.O.; Akpomie, K.G.; Conradie, J.; Adegoke, K.A. Advances in Supercapacitor Development: Materials, Processes, and Applications. *J. Electron. Mater.* **2023**, *52*, 96–129. [CrossRef]
3. Hu, X.; Zheng, W.; Wu, M.; He, Q.; Zhan, F.; Chen, L. Ternary layered double hydroxide cathode materials for electrochemical energy storage: A review and perspective. *Sustain. Energy Fuels* **2022**, *6*, 4551–4581. [CrossRef]
4. Liao, F.; Zhao, X.; Yang, G.; Cheng, Q.; Mao, L.; Chen, L. Recent advances on two-dimensional NiFe-LDHs and their composites for electrochemical energy conversion and storage. *J. Alloys Compd.* **2021**, *872*, 159649. [CrossRef]
5. Zhong, C.; Deng, Y.; Hu, W.; Qiao, J.; Zhang, L.; Zhang, J. A review of electrolyte materials and compositions for electrochemical supercapacitors. *Chem. Soc. Rev.* **2015**, *44*, 7484–7539. [CrossRef]
6. Choi, C.; Lee, J.M.; Kim, S.H.; Kim, S.J.; Di, J.; Baughman, R.H. Twistable and Stretchable Sandwich Structured Fiber for Wearable Sensors and Supercapacitors. *Nano Lett.* **2016**, *16*, 7677–7684. [CrossRef]
7. Zhu, G.; Xi, C.; Shen, M.; Bao, C.; Zhu, J. Nanosheet-Based Hierarchical $Ni_2(CO_3)(OH)_2$ Microspheres with Weak Crystallinity for High-Performance Supercapacitor. *ACS Appl. Mater. Interfaces* **2014**, *6*, 17208–17214. [CrossRef]
8. Zheng, J.P.; Cygan, P.J.; Jow, T.R. Hydrous Ruthenium Oxide as an Electrode Material for Electrochemical Capacitors. *J. Electrochem. Soc.* **1995**, *142*, 2699–2703. [CrossRef]
9. Azizi, S.; Seifi, M.; Moghadam, M.T.T.; Askari, M.B.; Varma, R.S. High-capacity $MnCo_2O_4/NiCo_2O_4$ as electrode materials for electrochemical supercapacitors. *J. Phys. Chem. Solids* **2023**, *174*, 111176. [CrossRef]
10. Mandal, S.; Hu, J.; Shi, S.Q. A comprehensive review of hybrid supercapacitor from transition metal and industrial crop based activated carbon for energy storage applications. *Mater. Today Commun.* **2023**, *34*, 105207. [CrossRef]
11. Tu, Q.; Zhang, Q.; Sun, X.; Wang, J.; Lin, B.; Chen, L.; Liu, J.; Deng, Z. Construction of three-dimensional nickel-vanadium hydrotalcite with ball-flower architecture for screen-printed asymmetric supercapacitor. *Appl. Surf. Sci.* **2023**, *615*, 156347. [CrossRef]
12. Jiao, Z.; Chen, Y.; Du, M.; Demir, M.; Yan, F.; Xia, W.; Zhang, Y.; Wang, C.; Gu, M.; Zhang, X.; et al. 3D hollow NiCo LDH nanocages anchored on 3D CoO sea urchin-like microspheres: A novel 3D/3D structure for hybrid supercapacitor electrodes. *J. Colloid Interface Sci.* **2023**, *633*, 723–736. [CrossRef] [PubMed]
13. Lu, Z.; Zhu, W.; Lei, X.; Williams, G.R.; O'Hare, D.; Chang, Z.; Sun, X.; Duan, X. High pseudocapacitive cobalt carbonate hydroxide films derived from CoAl layered double hydroxides. *Nanoscale* **2012**, *4*, 3640. [CrossRef]
14. Yan, W.; Zeng, H.-Y.; Zhang, K.; Long, Y.-W.; Wang, M.-X. Ni-Co-Mn hydrotalcite-derived hierarchically porous sulfide for hybrid supercapacitors. *J. Colloid Interface Sci.* **2023**, *635*, 379–390. [CrossRef] [PubMed]
15. Wang, H.; Tian, L.; Zhao, X.; Ali, M.; Yin, K.; Xing, Z. In situ growth MoS2/NiS composites on Ni foam as electrode materials for supercapacitors. *Mater. Today Commun.* **2023**, *34*, 105041. [CrossRef]
16. Chen, Q.; Huang, Z.; Zhao, W.; Tao, K.; Li, G.; Han, L. Hierarchical hybrid electrodes with $NiCo_2S_4$ nanosheets and Co_4S_3 nanocages for high energy density supercapacitors. *J. Alloys Compd.* **2023**, *937*, 168279. [CrossRef]
17. Jiang, T.; Zhang, Y.; Du, C.; Xiao, T.; Wan, L. Two-step electrodeposition synthesis of iron cobalt selenide and nickel cobalt phosphate heterostructure for hybrid supercapacitors. *J. Colloid Interface Sci.* **2023**, *629*, 1049–1060. [CrossRef]
18. Deshmukh, T.B.; Babar, P.; Kedara Shivasharma, T.; Sankapal, B.R. Mixed-valence iron phosphate: Superhydrophilic multi-plated microflakes towards symmetric supercapacitor. *Surf. Interfaces* **2022**, *35*, 102419. [CrossRef]
19. Tanwar, S.; Arya, A.; Sharma, A.L. $MoSe_2$-FeOOH nanocomposite as hybrid electrode material for high-performance symmetric supercapacitor. *Mater. Res. Bull.* **2023**, *160*, 112144. [CrossRef]
20. Zhang, M.; Jiang, D.; Jin, F.; Sun, Y.; Wang, J.; Jiang, M.; Cao, J.; Zhang, B.; Liu, J. Compression-tolerant supercapacitor based on $NiCo_2O_4/Ti_3C_2T_x$ MXene/reduced graphene oxide composite aerogel with insights from density functional theory simulations. *J. Colloid Interface Sci.* **2023**, *636*, 204–215. [CrossRef] [PubMed]
21. Mousavi Nakhodchari, M.; Seifi, M.; Tourchi Moghadam, M.T. Ternary $MnCo_2O_4$/MWCNT/rGO nanocomposites as high-performance supercapacitor electrode materials. *J. Phys. Chem. Solids* **2023**, *174*, 111170. [CrossRef]
22. Hu, B.; Chen, S.; Liu, S.; Wu, Q.; Yao, W.; Yu, S. Controllable Synthesis of Zinc-Substituted α- and β-Nickel Hydroxide Nanostructures and Their Collective Intrinsic Properties. *Chem. A Eur. J.* **2008**, *14*, 8928–8938. [CrossRef]
23. Shangguan, E.; Li, J.; Guo, D.; Guo, L.; Nie, M.; Chang, Z.; Yuan, X.-Z.; Wang, H. A comparative study of structural and electrochemical properties of high-density aluminum substituted α-nickel hydroxide containing different interlayer anions. *J. Power Sources* **2015**, *282*, 158–168. [CrossRef]
24. Wei, W.; Cui, S.; Ding, L.; Mi, L.; Chen, W.; Hu, X. Urchin-Like $Ni_{1/3}Co_{2/3}(CO_3)_{1/2}(OH)$ $0.11H_2O$ for Ultrahigh-Rate Electrochemical Supercapacitors: Structural Evolution from Solid to Hollow. *ACS Appl. Mater. Interfaces* **2017**, *9*, 40655–40670. [CrossRef]
25. Liu, Q.; Chen, Y.; Ma, J.; Xiong, X.; Zeng, X.; Qian, H. Novel electrochemical deposition of $Co(CO_3)_{0.5}(OH)\cdot_{0.11}H_2O$ nano-needles with folded umbrella-like architecture onto nickel foam for supercapacitors. *Surf. Coatings Technol.* **2021**, *421*, 127452. [CrossRef]
26. Sun, B.; Fan, X.; Hou, R.; Zhao, G.; Liu, Q.; Zhou, H.; Liang, P. Electrode made of NiCo double hydroxide on oxidized activated carbon for asymmetric supercapacitors. *Chem. Eng. J.* **2023**, *454*, 140280. [CrossRef]

27. Chen, L.; Zhao, X.; Tian, G.; Wei, Y.; Liu, T. Synthesis of NiCo-LDH@nitrogen-doped graphene hydrogel/nickel foam composites with 3D hierarchical structure for supercapacitors. *Mater. Lett.* **2023**, *334*, 133698. [CrossRef]
28. Zhang, M.; Liu, X.; Ma, M.; Ni, G.; Sun, Z.; Liu, J.; Wu, Y. 3D Hierarchical Urchin-Like $Ni_{0.3}Co_{0.6}Cu_{0.1}(CO_3)_{0.5}(OH)$ Microspheres for Supercapacitors with High Specific Capacitance. *Energy Fuels* **2021**, *35*, 20358–20366. [CrossRef]
29. Xiao, Q.; Yuan, Y.; Zhu, J.; Shi, Z.; Li, Z.; Zhu, J. Carbonate doped nickel-cobalt layered double hydroxide for high performance asymmetric supercapacitors. *J. Alloys Compd.* **2022**, *916*, 165391. [CrossRef]
30. Abouelamaiem, D.I.; He, G.; Parkin, I.; Neville, T.P.; Jorge, A.B.; Ji, S.; Wang, R.; Titirici, M.-M.; Shearing, P.R.; Brett, D.J.L. Synergistic relationship between the three-dimensional nanostructure and electrochemical performance in biocarbon supercapacitor electrode materials. *Sustain. Energy Fuels* **2018**, *2*, 772–785. [CrossRef]
31. Shewale, P.S.; Yun, K.-S. $NiCo_2O_4$/RGO Hybrid Nanostructures on Surface-Modified Ni Core for Flexible Wire-Shaped Supercapacitor. *Nanomaterials* **2021**, *11*, 852. [CrossRef] [PubMed]
32. Li, R.; Hu, Z.; Shao, X.; Cheng, P.; Li, S.; Yu, W.; Lin, W.; Yuan, D. Large Scale Synthesis of NiCo Layered Double Hydroxides for Superior Asymmetric Electrochemical Capacitor. *Sci. Rep.* **2016**, *6*, 18737. [CrossRef] [PubMed]
33. Fan, X.; Ohlckers, P.; Chen, X. One-Step and Morphology-Controlled Synthesis of Ni-Co Binary Hydroxide on Nickel Foam for High-Performance Supercapacitors. *Appl. Sci.* **2020**, *10*, 3814. [CrossRef]
34. Baek, S.-H.; Jeong, Y.-M.; Kim, D.Y.; Park, I.-K. Phase transformation of NiCo hydroxides derived from carbonate anion and its effect on electrochemical pseudocapacitor performance. *Chem. Eng. J.* **2020**, *393*, 124713. [CrossRef]
35. Chen, Y.; Fang, S.; Sun, L.; Xu, F.; Wang, M.; Zhang, J.; Mu, X.; Wang, X.; Wang, P.; Liu, J.; et al. Hierarchical $NiFe_2O_4$-NiAl-LDH arrays immobilized on activated carbon cloth for bifunctional application on high-performance supercapacitors and solar steam generation. *Sustain. Mater. Technol.* **2022**, *33*, e00500. [CrossRef]
36. Rieu, M.; Camara, M.; Tournier, G.; Viricelle, J.-P.; Pijolat, C.; de Rooij, N.F.; Briand, D. Fully inkjet printed SnO_2 gas sensor on plastic substrate. *Sensors Actuators B Chem.* **2016**, *236*, 1091–1097. [CrossRef]
37. Homenick, C.M.; James, R.; Lopinski, G.P.; Dunford, J.; Sun, J.; Park, H.; Jung, Y.; Cho, G.; Malenfant, P.R.L. Fully Printed and Encapsulated SWCNT-Based Thin Film Transistors via a Combination of R2R Gravure and Inkjet Printing. *ACS Appl. Mater. Interfaces* **2016**, *8*, 27900–27910. [CrossRef]
38. Simonenko, E.P.; Mokrushin, A.S.; Simonenko, N.P.; Voronov, V.A.; Kim, V.P.; Tkachev, S.V.; Gubin, S.P.; Sevastyanov, V.G.; Kuznetsov, N.T. Ink-jet printing of a TiO_2–10%ZrO_2 thin film for oxygen detection using a solution of metal alkoxoacetylacetonates. *Thin Solid Films* **2019**, *670*, 46–53. [CrossRef]
39. Sajedi-Moghaddam, A.; Rahmanian, E.; Naseri, N. Inkjet-printing technology for supercapacitor application: Current state and perspectives. *ACS Appl. Mater. Interfaces* **2020**, *12*, 34487–34504. [CrossRef]
40. Simonenko, T.L.; Simonenko, N.P.; Gorobtsov, P.Y.; Vlasov, I.S.; Solovey, V.R.; Shelaev, A.V.; Simonenko, E.P.; Glumov, O.V.; Melnikova, N.A.; Kozodaev, M.G.; et al. Microplotter printing of planar solid electrolytes in the CeO_2–Y_2O_3 system. *J. Colloid Interface Sci.* **2021**, *588*, 209–220. [CrossRef]
41. Simonenko, T.L.; Simonenko, N.P.; Simonenko, E.P.; Vlasov, I.S.; Volkov, I.A.; Kuznetsov, N.T. Microplotter Printing of Hierarchically Organized Planar $NiCo_2O_4$ Nanostructures. *Russ. J. Inorg. Chem.* **2022**, *67*, 1848–1854. [CrossRef]
42. Fedorov, F.S.; Simonenko, N.P.; Trouillet, V.; Volkov, I.A.; Plugin, I.A.; Rupasov, D.P.; Mokrushin, A.S.; Nagornov, I.A.; Simonenko, T.L.; Vlasov, I.S.; et al. Microplotter-Printed On-Chip Combinatorial Library of Ink-Derived Multiple Metal Oxides as an "Electronic Olfaction" Unit. *ACS Appl. Mater. Interfaces* **2020**, *12*, 56135–56150. [CrossRef]
43. Sobolewski, P.; Goszczynska, A.; Aleksandrzak, M.; Urbas, K.; Derkowska, J.; Bartoszewska, A.; Podolski, J.; Mijowska, E.; Fray, M. El A biofunctionalizable ink platform composed of catechol-modified chitosan and reduced graphene oxide/platinum nanocomposite. *Beilstein J. Nanotechnol.* **2017**, *8*, 1508–1514. [CrossRef] [PubMed]
44. Simonenko, T.L.; Simonenko, N.P.; Gorobtsov, P.Y.; Simonenko, E.P.; Kuznetsov, N.T. Microextrusion Printing of Multilayer Hierarchically Organized Planar Nanostructures Based on NiO, $(CeO_2)_{0.8}(Sm_2O_3)_{0.2}$ and $La_{0.6}Sr_{0.4}Co_{0.2}Fe_{0.8}O_{3-\delta}$. *Micromachines* **2022**, *14*, 3. [CrossRef] [PubMed]
45. Simonenko, T.L.; Simonenko, N.P.; Gorobtsov, P.Y.; Grafov, O.Y.; Simonenko, E.P.; Kuznetsov, N.T. Synthesis of $((CeO_2)_{0.8}(Sm_2O_3)_{0.2})$@NiO Core-Shell Type Nanostructures and Microextrusion Printing of a Composite Anode Based on Them. *Materials* **2022**, *15*, 8918. [CrossRef]
46. Gorobtsov, P.Y.; Mokrushin, A.S.; Simonenko, T.L.; Simonenko, N.P.; Simonenko, E.P.; Kuznetsov, N.T. Microextrusion Printing of Hierarchically Structured Thick V_2O_5 Film with Independent from Humidity Sensing Response to Benzene. *Materials* **2022**, *15*, 7837. [CrossRef]
47. Fisenko, N.A.; Solomatov, I.A.; Simonenko, N.P.; Mokrushin, A.S.; Gorobtsov, P.Y.; Simonenko, T.L.; Volkov, I.A.; Simonenko, E.P.; Kuznetsov, N.T. Atmospheric Pressure Solvothermal Synthesis of Nanoscale SnO_2 and Its Application in Microextrusion Printing of a Thick-Film Chemosensor Material for Effective Ethanol Detection. *Sensors* **2022**, *22*, 9800. [CrossRef]
48. Simonenko, N.P.; Kadyrov, N.S.; Simonenko, T.L.; Simonenko, E.P.; Sevastyanov, V.G.; Kuznetsov, N.T. Preparation of ZnS Nanopowders and Their Use in the Additive Production of Thick-Film Structures. *Russ. J. Inorg. Chem.* **2021**, *66*, 1283–1288. [CrossRef]
49. Seo, H.; Nishi, T.; Kishimoto, M.; Ding, C.; Iwai, H.; Saito, M.; Yoshida, H. Study of Microextrusion Printing for Enlarging Electrode–Electrolyte Interfacial Area in Anode-Supported SOFCs. *ECS Trans.* **2019**, *91*, 1923–1931. [CrossRef]

50. Simonenko, T.L.; Simonenko, N.P.; Gorobtsov, P.Y.; Mokrushin, A.S.; Solovey, V.R.; Pozharnitskaya, V.M.; Simonenko, E.P.; Glumov, O.V.; Melnikova, N.A.; Lizunova, A.A.; et al. Pen plotter printing of Co_3O_4 thin films: Features of the microstructure, optical, electrophysical and gas-sensing properties. *J. Alloys Compd.* **2020**, *832*, 154957. [CrossRef]
51. Mokrushin, A.S.; Fisenko, N.A.; Gorobtsov, P.Y.; Simonenko, T.L.; Glumov, O.V.; Melnikova, N.A.; Simonenko, N.P.; Bukunov, K.A.; Simonenko, E.P.; Sevastyanov, V.G.; et al. Pen plotter printing of ITO thin film as a highly CO sensitive component of a resistive gas sensor. *Talanta* **2021**, *221*, 121455. [CrossRef]
52. Simonenko, T.L.; Simonenko, N.P.; Gorobtsov, P.Y.; Pozharnitskaya, V.M.; Simonenko, E.P.; Glumov, O.V.; Melnikova, N.A.; Sevastyanov, V.G.; Kuznetsov, N.T. Pen Plotter Printing of MnOx Thin Films Using Manganese Alkoxoacetylacetonate. *Russ. J. Inorg. Chem.* **2021**, *66*, 1416–1424. [CrossRef]
53. Kokulnathan, T.; Wang, T.-J.; Ahmed, F.; Arshi, N. Fabrication of flower-like nickel cobalt-layered double hydroxide for electrochemical detection of carbendazim. *Surf. Interfaces* **2023**, *36*, 102570. [CrossRef]
54. Su, W.; Wu, F.; Fang, L.; Hu, J.; Liu, L.; Guan, T.; Long, X.; Luo, H.; Zhou, M. NiCo-LDH nanowires@nanosheets core-shell structure grown on carbon fiber cloth for high performance flexible supercapacitor electrode. *J. Alloys Compd.* **2019**, *799*, 15–25. [CrossRef]
55. Porta, P.; Dragone, R.; Fierro, G.; Inversi, M.; Jacono, M.L.; Moretti, G. Preparation and characterisation of cobalt–copper hydroxysalts and their oxide products of decomposition. *J. Chem. Soc. Faraday Trans.* **1992**, *88*, 311–319. [CrossRef]
56. Zhou, T.; Gao, W.; Wang, Q.; Umar, A. Effect of Fluoride on the Morphology and Electrochemical Property of Co_3O_4 Nanostructures for Hydrazine Detection. *Materials* **2018**, *11*, 207. [CrossRef]
57. Wu, J.; Mi, R.; Li, S.; Guo, P.; Mei, J.; Liu, H.; Lau, W.-M.; Liu, L.-M. Hierarchical three-dimensional $NiCo_2O_4$ nanoneedle arrays supported on Ni foam for high-performance supercapacitors. *RSC Adv.* **2015**, *5*, 25304–25311. [CrossRef]
58. Yang, S.; Zhang, Z.; Zhou, J.; Sui, Z.; Zhou, X. Hierarchical NiCo LDH–rGO/Ni Foam Composite as Electrode Material for High-Performance Supercapacitors. *Trans. Tianjin Univ.* **2019**, *25*, 266–275. [CrossRef]
59. Wang, J.; Gao, F.; Du, X.; Ma, X.; Hao, X.; Ma, W.; Wang, K.; Guan, G.; Abudula, A. A high-performance electroactive PPy/rGO/NiCo-LDH hybrid film for removal of dilute dodecyl sulfonate ions. *Electrochim. Acta* **2020**, *331*, 135288. [CrossRef]
60. Abitkar, S.B.; Dhas, S.D.; Jadhav, N.P.; Jadhav, P.R.; Maldar, P.S.; Patil, C.E.; Moholkar, A.V. Enhanced specific capacitance and electrochemical properties of nickel hydroxide-activated carbon (α-$Ni(OH)_2$–AC) nanocomposite for pseudocapacitor electrode material. *J. Mater. Sci. Mater. Electron.* **2021**, *32*, 8657–8667. [CrossRef]
61. Bion, N.; Saussey, J.; Hedouin, C.; Seguelong, T.; Daturi, M. Evidence by in situ FTIR spectroscopy and isotopic effect of new assignments for isocyanate species vibrations on Ag/Al_2O_3. *Phys. Chem. Chem. Phys.* **2001**, *3*, 4811–4816. [CrossRef]
62. Wang, H.; Wang, M.; Zhao, W.; Wei, W.; Sun, Y. Reaction of zinc oxide with urea and its role in urea methanolysis. *React. Kinet. Mech. Catal.* **2010**, *99*, 381–389. [CrossRef]
63. Huang, J.; Hu, Q.; Guo, X.; Zeng, Q.; Wang, L. Rethinking $Co(CO_3)_{0.5}(OH)$ $0.11H_2O$: A new property for highly selective electrochemical reduction of carbon dioxide to methanol in aqueous solution. *Green Chem.* **2018**, *20*, 2967–2972. [CrossRef]
64. Li, S.; Wang, L.; Li, Y.; Zhang, L.; Wang, A.; Xiao, N.; Gao, Y.; Li, N.; Song, W.; Ge, L.; et al. Novel photocatalyst incorporating Ni-Co layered double hydroxides with P-doped CdS for enhancing photocatalytic activity towards hydrogen evolution. *Appl. Catal. B Environ.* **2019**, *254*, 145–155. [CrossRef]
65. Wang, J.; Luo, Y.; Ling, L.; Wang, X.; Cui, S.; Li, Z.; Jiao, Z.; Cheng, L. Sandwich-like NiCo-LDH/rGO with rich mesopores and high charge transfer capability for flexible supercapacitors. *CrystEngComm* **2022**, *24*, 4962–4974. [CrossRef]
66. Zhang, C.; Zhang, L.; Liu, Q.; Ding, Y.; Cheng, L.; Wu, M.; Li, Z. Enhanced interfacial electron transfer by constructing NiCo-LDH hollow nanocages decorated N-doped graphene quantum dots heterojunction for high-performance supercapacitors. *Appl. Surf. Sci.* **2022**, *602*, 154352. [CrossRef]
67. Guo, Y.; Hong, X.; Wang, Y.; Li, Q.; Meng, J.; Dai, R.; Liu, X.; He, L.; Mai, L. Multicomponent Hierarchical Cu-Doped NiCo-LDH/CuO Double Arrays for Ultralong-Life Hybrid Fiber Supercapacitor. *Adv. Funct. Mater.* **2019**, *29*, 1809004. [CrossRef]
68. Bhojane, P.; Sinha, L.; Goutam, U.K.; Shirage, P.M. A 3D mesoporous flowers of nickel carbonate hydroxide hydrate for high-performance electrochemical energy storage application. *Electrochim. Acta* **2019**, *296*, 112–119. [CrossRef]
69. Guellati, O.; Harat, A.; Momodu, D.; Dangbegnon, J.; Romero, T.; Begin, D.; Pham-Huu, C.; Manyala, N.; Guerioune, M. Electrochemical measurements of 1D/2D/3DNi-Co bi-phase mesoporous nanohybrids synthesized using free-template hydrothermal method. *Electrochim. Acta* **2018**, *275*, 155–171. [CrossRef]
70. Ramachandran, R.; Lan, Y.; Xu, Z.-X.; Wang, F. Construction of NiCo-Layered Double Hydroxide Microspheres from Ni-MOFs for High-Performance Asymmetric Supercapacitors. *ACS Appl. Energy Mater.* **2020**, *3*, 6633–6643. [CrossRef]
71. Kurra, N.; Alhebshi, N.A.; Alshareef, H.N. Microfabricated Pseudocapacitors Using $Ni(OH)_2$ Electrodes Exhibit Remarkable Volumetric Capacitance and Energy Density. *Adv. Energy Mater.* **2015**, *5*, 1401303. [CrossRef]
72. Lu, H.; Chen, J.; Tian, Q. Wearable high-performance supercapacitors based on Ni-coated cotton textile with low-crystalline Ni-Al layered double hydroxide nanoparticles. *J. Colloid Interface Sci.* **2018**, *513*, 342–348. [CrossRef] [PubMed]